Free-Space Permittivity Measurement at Terahertz Frequencies With a Vector Network Analyzer

Jonathan Hammler, *Student Member, IEEE*, Andrew J. Gallant, *Member, IEEE*, and Claudio Balocco, *Member, IEEE*

Abstract—A simple system, based on a vector network analyzer, has been used with new numerical de-embedding and parameter inversion techniques to determine the relative permittivity (dielectric properties) of materials within the frequency range 750–1100 GHz. Free-space (noncontact), nondestructive testing has been performed on various planar dielectric and semiconducting samples. This system topology is well suited for quality control testing in an industrial setting requiring high throughput. Scattering parameters, measured in the absence of a sample, were used to computationally move the measurement plane to the surface of the samples being characterized. This de-embedding process can be completed much faster than a traditional calibration process and does not require exact knowledge of system geometric lengths. An iterative method was developed for simultaneously determining both sample geometric thickness and electric permittivity, through calculation of theoretical scattering parameters at material boundaries. A constrained nonlinear optimization process was employed to minimize the discrepancy between measured transmission and reflection data with this simulated data, in lieu of a closed-form parameter inversion algorithm. Monte Carlo simulations of parameter retrieval in the presence of artificial noise have demonstrated our method's robustness and superior noise rejection compared with a noniterative method. The precision of derived results has been improved by a factor of almost 50, compared to a closed-form extraction technique with identical input.

Index Terms—Free-space, frequency-domain analysis, measurement uncertainty, nondestructive testing, numerical analysis, permittivity.

I. INTRODUCTION

WHILE often referred to as the *dielectric constant*, permittivity (ϵ_r) can only be considered constant for a single frequency. However, for overdefined intervals of the frequency spectrum, its value may be treated as constant where a material is nondispersive. For many dielectrics applicable to usage in terahertz (THz) devices, subtle variations in processing parameters or molecular structure during polymer manufacturing result in permittivity deviating from the nominal value. Similarly, for semiconductors, permittivity is a function of conductivity and doping/carrier concentration.

As permittivity dictates the interaction of an electromagnetic (EM) wave with a device's geometry, its value must be known during the design process. While dielectric properties of many materials have been extensively characterized at low frequencies and into the microwave region of the EM spectrum, published information is still much sparser for applications within the THz region. Correct operation of such THz devices (e.g., lenses, diffractive optics, filters, waveguides, etc.) then relies upon the manufacturer's ability to keep critical process parameters within acceptable control limits. With variations between batches of stock material resulting in reduced yield, we aim to simplify and speed up the process of determining the relative permittivity for planar substrates in the THz region of the frequency spectrum. There are two well-known techniques for characterizing dielectrics: time-domain spectroscopy (TDS) [1] and, for lower frequency ranges, measurements taken with a vector network analyzer (VNA) [2]. TDS topologies provide large bandwidth for measurements, but require a large number of optical components—occupying a large space—with a femtosecond-pulsed laser, all of which will require aligning. The bandwidth and resolution of TDS systems also require relatively long scan times while an optical delay line is repositioned. While occasionally coupled into a waveguide [3], either rectangular or on-chip, most time-domain systems currently operate in free-space. Free-space methods can be noncontact and nondestructive, while samples prepared for insertion into a waveguide must be cut to size. Similarly, an on-chip TDS system would require patterning and modification of sample surfaces.

Regardless of measurement system, sample thickness must then be ascertained through measurements with a micrometer (or similar instrument). This measured value, along with transmission and/or reflection measurements within the frequency range of interest, is processed to calculate the material's relative permittivity. This paper presents a computational method to extract a dielectric characterization, which does not require an accurate measurement of geometry to be first performed.

A system employing a VNA and fast Schottky diode-based frequency converters [4] has been assembled to measure the scattering parameters of planar samples directly in the frequency domain. The number of optical components required are significantly smaller than that of TDS systems, reducing system complexity. As shown in Fig. 1(a), only two parabolic mirrors and a sample holder must be aligned with a pair of horn antennas. No laser is required and the effect of drift within the system is minimized due to shorter optical path lengths and a lack of moving components. A method was developed to numerically recalibrate the system, which takes only a few seconds, with greater ease than traditional methods; requirements on accurate
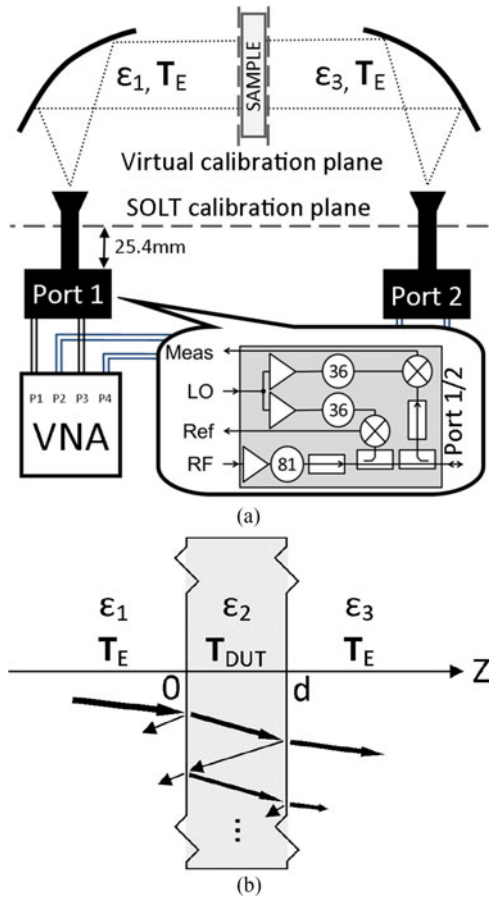
Fig. 1.   (a) Symmetric layout of measurement system showing the location of calibration planes. Inset: VDI THz frequency extender (WR1.0) block diagram. (b) Schematic version of transmission path for de-embedding algorithm.

positioning of the sample have been relaxed. Only orthogonality between sample surface and incident radiation must be maintained to a high degree of accuracy.

The iterative technique presented in this paper simultaneously determines the exact geometric thickness and relative permittivity of planar samples from scattering (S-) parameters. Results from semiconductor and dielectric samples, showing excellent agreement with prior work, are presented in Section III. Finally, an investigation into the robustness of the method in the presence of measurement noise was performed.

II. Methodology

A. Experimental Apparatus

The measurement setup is shown in Fig. 1(a). A pair of off-axis parabolic mirrors was used to collect, collimate, and focus a THz beam emitted from horn antennas mounted on Virginia Diodes (VDI) frequency extension modules. These devices contain Schottky diode frequency doublers, triplers, and subharmonic mixers to upconvert local oscillator and radio frequency inputs generated by two VNA ports to the desired output frequency. Similarly, input to the test port is downconverted to a frequency range measurable by the VNA.

A four-port VNA is converted into a two-port network analyzer operating at THz frequencies. The optical path length was approximately 30 cm, with a 2 in diameter mounting bracket located at the midpoint for sample retention. All material samples were 50 mm in diameter, which was found to be sufficiently larger than the 6-mm wide collimated probing beam. An iris or aperture can be placed, sacrificing dynamic range and, therefore, signal-to-noise ratio (SNR) to measure smaller samples in the collimated beam, while satisfying the assumption that samples extend to infinity in the XY plane. Alternatively, parabolic mirrors or lenses may be employed to refocus the radiation with the sample holder located at the beam waist.

After the frequency extension transceivers were connected to the VNA, short, open, load, and through WR1.0 waveguide standards were used to calibrate the measurement equipment. Short, open, load, and through (SOLT) calibration accounts for systematic errors between VNA receivers and waveguide flanges. A numeric de-embedding technique then removes noise and other phase shift effects introduced between the flanges and the sample surface, as shown in Section II-B.

Two-port S-parameter measurements were made with the VNA (Keysight N5224A). During the measurement process, the position and direction of the mirrors were adjusted such that the magnitude of transmission (S21 or S12, which are equivalent due to the symmetric layout of the system) between antennas was at a maximum. Theoretically, this maximum is limited by absorption of THz radiation by the air it propagates through, which is small due to the lack of water absorption lines within the measurement frequency range. This makes accuracy of alignment the dominant factor in determining the maximum signal intensity and, therefore, dynamic range of the measurement. Subsequently, a reflective aluminum plate was mounted in the sample holder. Tip and tilt adjustments were made to the holder in order to maximize reflection S-parameters S11 and S22. An increase in S11 is often accompanied by a decrease in S21 (and vice versa), due to incident and transmitted ray bundles remaining parallel (Snell's law of refraction) while reflections leave the paraxial beam at an angle equal to the angle of incidence. Additionally, the six degrees of freedom provided by each post and mirror mount are not completely decoupled from each other: adjustments needed to be made iteratively until both reflection parameters and transmission were at a maximum, signifying that the collimated beam was travelling perpendicular to both front and back surfaces of the sample plate, and the majority of energy emitted was collected after interacting with the sample under test. Once adequate system alignment was achieved, measurement of two-port scattering parameters was performed between 750 and 1100 GHz, with an intermediate frequency bandwidth (IFBW), used for bandpass filtering the received signal, of 100 Hz. Narrow IFBW values result in reduced noise and longer measurement sweep times. Averaging of multiple sweeps was implemented to further reduce the effect of random noise. Averaging three sweeps was chosen as a suitable tradeoff between increased accuracy and increased measurement time.

B. Numeric De-Embedding of Sample Response

The measured geometry has been mathematically modeled as three stratified regions, each with differing EM propagation parameters [wave impedance η_Z as in (5) and wavenumber k_Z as in (6)] in series, as shown by the transmission parameter matrices in (1). Fig. 1(b) illustrates the arrangement of a central volume filled either by the sample under test or air (represented by the transmission matrices $\mathbf{T}_{\text{DUT}}$ and $\mathbf{T}_{\text{air}}$, respectively), flanked by $\mathbf{T}_E$, where EM radiation is coupled between a waveguide and free-space with a diagonal horn antenna. $\mathbf{T}_E$ models the space between sample and the SOLT calibration plane of the VNA

$$\mathbf{T}_{\text{measured}} = \mathbf{T}_E \cdot \mathbf{T}_{\text{DUT}} \cdot \mathbf{T}_E \tag{1}$$

$$\mathbf{A} = \mathbf{T}_{\text{air}}^{-1} \cdot \sqrt{\mathbf{T}_{\text{air}} \cdot \mathbf{T}_{\text{empty}}} \tag{2}$$

$$\mathbf{T}_{\text{DUT}} = \mathbf{A}^{-1} \cdot \mathbf{T}_{\text{measured}} \cdot \mathbf{A}^{-1}. \tag{3}$$

$\mathbf{T}_{\text{empty}}$ represents the S-parameter response of the system without a sample in place, converted to ABCD-parameters for ease of calculation. It is used as a reference measurement for the normalization procedure. $\mathbf{T}_{\text{measured}}$ contains the S-parameter measurements taken with a sample in place. $\mathbf{T}_{\text{air}}$ is calculated from (4), the scattering matrix for an idealized section of air of length d, in the usual fashion [5]

$$\mathbf{S}_{\text{air}} = \begin{pmatrix} 0 & e^{-j2\pi df} \\ e^{-j2\pi df} & 0 \end{pmatrix}. \tag{4}$$

Equation (3) expresses the effect of sample insertion, normalized against the measurement system with the sample absent, while assuming $\mathbf{T}_E$ remains constant between the two measurement sweeps.

Recording a set of S-parameter measurements, to calculate $\mathbf{T}_{\text{empty}}$, is significantly faster than performing a through, reflect, line calibration [6], allowing for samples of differing thicknesses to be quickly and accurately characterized without performing additional precision measurement and calibration steps. The de-embedding matrix transformation can be adapted to eliminate the effects of different mounting jigs or conveyor belt of known thickness and permittivity by accounting for their interaction with the probing beam.

C. Parameter Inversion Through Iterative Simulations

After the scattering parameters of the material under test were determined, the real components of relative permittivity and sample thickness were simultaneously determined with a constrained nonlinear optimization algorithm. The method was implemented in MATLAB such that it could be run on either a multicore desktop computer or split across a cluster of workers in parallel. The algorithm used for minimizing (9) is an "active-set" (*projection method*) based solver as described by Gill *et al.* [7], [8]. At each iteration, an approximation is made of the Hessian matrix of the Lagrangian function, using the quasi-Newtonian formula of Broyden, Fletcher, Goldfarb, Shanno [9]. The solution to this quadratic subproblem is used to choose the direction of travel for a line search procedure. The step-size used in this search is determined to produce a sufficient decrease of a

merit function of the form used by Han [10] and Powell [11]. A scatter-search method [12] has been implemented to eliminate solutions, which are not a global minima.

Relative permittivity and thickness values were drawn from ranges of acceptable values and input as parameters to a matrix representation of a Fabry–Perot etalon. From many combinations of viable thickness and permittivity values, simulations generate S-parameter matrices, which are compared with the measured scattering response of the sample, determined by the de-embedding process described in Section II-B

$$\eta_X = \sqrt{\frac{j\omega\mu_0\mu_{r_X}}{\sigma + j\omega\epsilon_0\epsilon_{r_X}}} \approx \frac{377\,\Omega}{\sqrt{\epsilon'_{r_X}}} \tag{5}$$

$$k_X = \frac{2\pi\sqrt{\epsilon_{r_X}}}{\lambda_0} \tag{6}$$

$$\mathbf{E}(z) = E_0 \cdot e^{-jkz} \tag{7}$$

where X denotes the relevant stratified region

$$X = \begin{cases} 1, & \text{if } z < 0 \\ 2, & \text{if } 0 \le z \le d \\ 3, & \text{if } z > d. \end{cases}$$

Maxwell's equations dictate that continuity of electric and magnetic field vectors must be maintained at interfaces. As our measurement geometry utilizes a low-divergence Gaussian beam, the electric field $\mathbf{E}$ is related to the magnetic field $\mathbf{H}$ through the impedance of free space $Z_0 = \sqrt{\frac{\mu_0}{\epsilon_0}} = 377\,\Omega$ and the refractive index of the nonmagnetic material ($n = \sqrt{\epsilon_r\mu_r})|_{\mu_r=1}$. The magnitude and phase of magnetic and electric field vectors were found at each boundary by summing forward and reverse traveling waves, modeled as exponential functions as in 7 with a purely real propagation constant k: the assumption that the sample is a lossless, perfect dielectric is made to reduce calculation complexity. A more rigorous calculation results in a complex propagation constant for $\mathbf{E}, \mathbf{H}$ waves when using $\eta = \sqrt{\frac{j\omega\mu_0\mu_r}{\sigma + j\omega\epsilon_0\epsilon_r}}$ to calculate field amplitude and phase at each boundary. An extra degree of freedom is added to the problem by including the conductivity of the sample. Additionally, for magnetic materials, permeability $\mu_r \ne 1$ introduces yet another. In general, each additional Lorentz–Drude oscillator term contributes another degree of freedom to the optimization problem. The assumption of the sample under test being nondispersive has been made so that the frequency dependence is removed from $\sqrt{\epsilon_{2_X}(f)}$ in (5) and (6).

Maxwell's equations, which dictate that fields must be continuous at interfaces, were utilized to calculate field amplitude and phase at each interface. The matrix formulation of the four boundary conditions is shown in (8), where the top two rows of $\mathbf{A}$ correspond to electric field continuity and the bottom two

rows correspond to magnetic field continuity

$$
\mathbf{A} = \begin{bmatrix}
1 & -1 & -1 & 0 \\
0 & e^{-ik_2 d} & e^{ik_2 d} & -e^{-ik_3 d} \\
-1/\eta_1 & -1/\eta_2 & 1/\eta_2 & 0 \\
0 & e^{-ik_2 d}/\eta_2 & -e^{ik_2 d}/\eta_2 & -e^{-ik_3 d}/\eta_3
\end{bmatrix}. \quad (8)
$$

The system of equations formed from the product

$$
\mathbf{A} \cdot \begin{bmatrix} S11 \\ \vdots \\ S21 \end{bmatrix} = \begin{bmatrix} -E_{1F} \\ 0 \\ -E_{1F}/\eta_1 \\ 0 \end{bmatrix}
$$

has been solved with the amplitude of forward-traveling incident radiation $E_{1F} = 1$ to find S11 (the relative amplitude of reflection at the front face) and S21 (transmission out of the rear face)—the scattering parameters of the material being simulated.

The residual sum of squares was used to quantify the difference between measured and simulated S-parameters. This metric, shown with S21 in (9) and (10), was minimized to find the combination of permittivity and thickness, which results in a transmission spectrum which best fits the measured data

$$
\text{Error} = \sum_f |S21_{\text{sim}} - S21_{\text{MUT}}|^2 \quad (9)
$$

$$
S21_{\text{sim}} = \frac{4\eta_2\eta_3 e^{jdk_3}}{\eta_1\eta_2 - \eta_1\eta_3 + \eta_2\eta_3 - \eta_2^2}
$$
$$
+(\eta_1\eta_2 + \eta_1\eta_3 + \eta_2^2 + \eta_2\eta_3)e^{j2dk_2}. \quad (10)
$$

The forward transmission coefficient S21 was found to have a larger SNR and a lower variance than reflectance coefficients, as outlined in Section III, which results in increased accuracy of answers. When the difference is small, that is to say the quality of fit (determined by R^2, the coefficient of determination) is deemed high enough, the values of the input parameters can be ascribed to those of the sample under test. Initial estimates of both parameters are required, however their proximity to final values is unimportant as a multiple-start global search is performed to eliminate the risk of finding only a local minima. As a consequence, initial estimates take the form of ranges of possible values, from which initial guesses can be drawn pseudorandomly. For example, fitted thickness values were constrained to either the confidence interval of measured sample thicknesses, or to a manufacturer-provided tolerance band around a nominal value.

III. RESULTS AND DISCUSSION

Our measurement method has been utilized to obtain the results presented in Table I, alongside values obtained from measurements of material samples at gigahertz and THz frequencies—where available. Some common substrates for THz devices have been characterized. In addition to the deviations in measured values experienced by multiple groups measuring the same standard [13], discrepancies in value between measured permittivity and other works arise due to dissimilar,

TABLE I
PERMITTIVITY (ϵ_r') AND THICKNESS (d) VALUES OF TESTED SAMPLES,
WITH A COMPARISON TO PREVIOUSLY REPORTED WORK

Material	ϵ_r'	$d\,(\mu\text{m})$	R^2	ϵ_r' Other Works
Silicon	11.19	286	0.982	11.7 [14]
HR-Si	11.57	500	0.990	11.7 [15]
HR-GaAs	13.01	348	0.981	12.9 [15]
Polystyrene	02.45	749	0.972	02.9 [16]

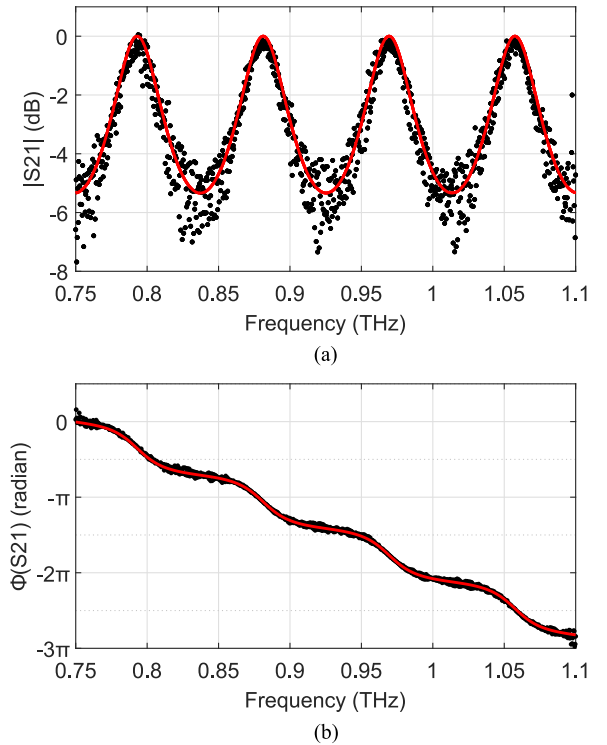$f_c = 0.925$ THz. HR=High-resistivity.

(a)

(b)

Fig. 2.   Bode plot of forward transmission (a) magnitude and (b) phase through a high-resistivity silicon wafer sample. Dots: measured data. Solid lines: fitted curves ($d = 500.2\,\mu$m, $\epsilon_r = 11.58$) $R^2 = 0.990$.

physically distinct samples being compared. However, in general, there is good agreement between our results and the values obtained from the literature.

A typical complex transmission measurement and associated fitted curves are plotted in Fig. 2. The raw measurement data from these experiments have also been used in Section III-A for an uncertainty analysis and evaluation of precision.

Sample thicknesses were first obtained with a single measurement, performed with callipers ($\pm 10\,\mu$m), as an initial guess for the optimization algorithm. Thickness values obtained from the iterative fitting process were found to be an order of magnitude more precise than initial measurements, and accuracy was verified against the distribution of 30 μm ($\pm 1\,\mu$m) measurements of each sample.

A. Precision of Results

In order to assess the level of precision realized with our method, the variance in measured quantities was quantified and

characterized. Synthetic noise was generated and superimposed on measured data. Multiple algorithms were then utilized to calculate permittivity and the Monte Carlo method was employed to find the variance in output quantities in the presence of noise. This well-documented technique has been used to propagate the known uncertainty of input signals through both the recalibration and parameter inversion algorithms. This methodology was applied in lieu of a sensitivity analysis based upon partial-derivatives so that the nonlinear optimization function can be considered as a *black box* [17]. An analysis was performed of the probability distribution of fitted parameters output from the simulations. The standard deviation of the distributions has been used as a metric to determine the level of precision, which can be reliably obtained from our method.

In order to introduce perturbations to the system model that accurately reflects the nature of noise inherent to that system, the variance in input quantities was first measured and compared with device specifications. About 3000 S-parameter readings were taken at multiple fixed frequencies. Quantile plots and probability density functions (PDFs) of real and imaginary measurement components were found to show the data following a Gaussian distribution [18], as is expected of additive noise. Correlation coefficients between each S-parameter's noise are approximately zero (lower adjacent $= -0.031$, upper adjacent $= 0.023$), so univariate normal distributions have used to represent the additive noise present in addition to the measurement. Errors have been measured and presented in linear terms to prevent asymmetric noise being calculated after converting from dB [18]. A principal component analysis was performed to find the magnitude of the standard deviation of this noise. The length of the colored lines in Fig. 3 indicate this magnitude, while the angle corresponds to the direction of the principal axis. These magnitudes are equal to a tolerance of $\pm 3\%$, typically within 1%. Fig. 3 shows the worst-case scenario, at $f = 1.1$ THz, where the dynamic range of the VDI frequency extender modules and VNA is limited [4]. The distributions of reflection measurements S11 and S22 are offset from zero due to the contribution of energy reflected at the interface where each antenna is mounted to a waveguide flange. This mounting misalignment has been reduced with the inclusion of alignment pins in the mating surfaces. However, prior work has demonstrated that this mismatch, which occurs past our SOLT calibration plane in Fig. 1(a), is inherent to the process of aligning two $250 \times 125\ \mu\text{m}$ apertures centered on $4\ \text{cm}^2$ flanges [19]. The unrepeatable nature of this error required a significant number of measurements to be performed under identical conditions with the horn antennas periodically removed and reinstalled. After characterizing the noise affecting the reflection coefficients, its magnitude was incorporated into the Monte Carlo simulation model. This noise has been accounted for in measurements by our numeric recalibration process, as discussed in Section II-B. Increasing the number of sweeps included in the mean empty-system response, used as the recalibration reference measurement, more accurately represents the contribution of this error term; however, analysis shows that the relative variation in magnitudes is small with $\sigma(S_{\text{nn}}) \approx -58$ dB. An additional error is introduced by any angular misalignment between sample
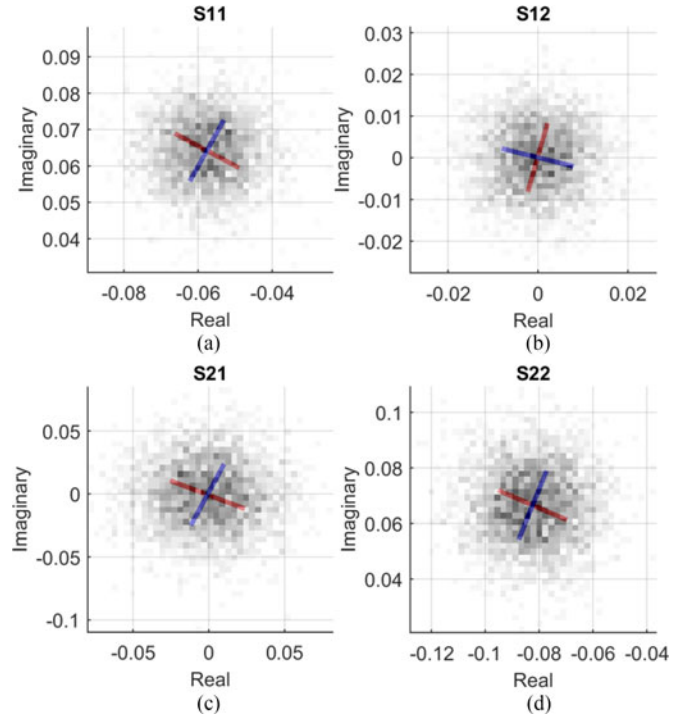

Fig. 3. Principal component analysis showing direction and magnitude of standard deviation of S-parameter measurements made at 1.1 THz. Plotted on equal, linear axes, the points follow a normal (Gaussian) distribution with imaginary and real components having equal variance.

normal and optical axis. While transmission through the sample remains on-axis, reflections diverge by the incidence angle and may not be collected by the mirrors. For these reasons, (9) considers only S21. S11/S22 are simulated for verification purposes only.

Noise in thickness measurements was drawn from a normal distribution when mean and standard deviation of the measurements was known. This occurred when a series of micrometer measurements of samples were made. When only a confidence interval or range of possible thickness values was known, values were generated from a rectangular distribution across the interval.

The datasets obtained from measuring the samples listed in Section III were subjected to the addition of random noise drawn from the probability distributions described above. The data were then processed with our recalibration and parameter inversion method. After logging the fitted parameters and quality of fit, the simulation was repeated until a statistically significant number of results were obtained for analysis.

Results from the Monte Carlo simulations show both the precision of our algorithm and the robustness of the iterative fitting method. Table II contains information characterizing the PDFs obtained from processing the perturbed datasets with our iterative algorithm and a closed-form equation approach. The standard deviation of fitted permittivity values in the presence of simulated noise is very small. While the noniterative process was found to follow a univariate Gaussian distribution (as did the input noise), plots of probability density from our

TABLE II
COMPUTED STANDARD DEVIATION (σ) AND 95% CONFIDENCE INTERVAL (CI) RESULTS FROM 30 000 ITERATIONS OF
MONTE CARLO SIMULATIONS ADDING RANDOM NOISE TO MEASURED SAMPLE DATA

Sample	Iterative Method		Noniterative Method	
	$\sigma(\epsilon_r')$	ϵ_r' 95% CI	$\sigma(\epsilon_r')$	ϵ_r' 95% CI
Silicon	2.0885×10^{-3}	$[11.18001, 11.18902]$	107.54×10^{-3}	$[10.79749, 11.22042]$
HR-Si	1.5870×10^{-3}	$[11.57170, 11.57840]$	68.292×10^{-3}	$[11.87660, 12.14389]$
HR-GaAs	5.2666×10^{-3}	$[13.01009, 13.02960]$	107.52×10^{-3}	$[12.82926, 13.25133]$
Polystyrene	0.17506×10^{-3}	$[02.47135, 02.47203]$	4.6952×10^{-3}	$[02.45781, 02.47631]$

$f_c = 0.925$ THz. Parameters were inverted using a noniterative method [20] for comparison. HR = High-resistivity. Iterative $\overline{\epsilon_r'}$ listed in Table I. Noniterative $\overline{\epsilon_r'}$ located at center of CI.
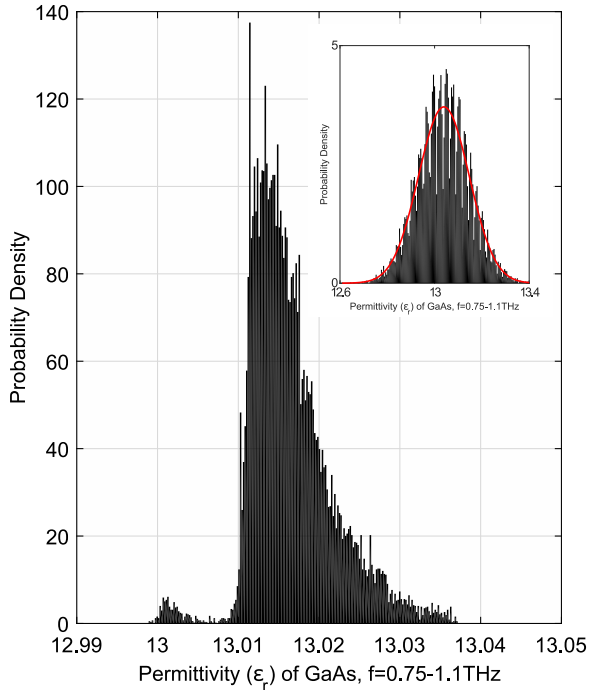

Fig. 4.   Probability density of fitted permittivity values of a gallium arsenide (GaAs) wafer from Monte Carlo simulation of additive noise. Inset: PDF of identical data processed with a noniterative method. Solid red line: normal distribution with $\mu = 13.039, \sigma = 0.1075$.

iterative system show distinct peaks, where a local minimum has been selected as the most likely fit to the data. This behavior is illustrated in Fig. 4.

The mean and standard deviation of each distribution have been measured. Confidence intervals have been calculated empirically by integration of the obtained PDF. Other characteristics of these distributions, such as kurtosis and skewness, have been investigated.

A comparison has been made with identical data subjected to the same noise, but with permittivity found with a noniterative method [20]. This method assumes that the sample thickness is known exactly. Confidence intervals were found by numerically integrating the cumulative distribution function of the Monte Carlo results to find the bounds of the lower and upper 2.5% of fitted permittivity values. The 95% confidence intervals of our method were found to be between 20 and 50 times smaller, indicating that the inversion process is much more resilient to the effect of measurement noise.

A qualitative evaluation of fitting behavior was performed by analyzing the shape of ϵ_r' PDFs. Results obtained from noniterative processing were found to have skew in the range $[0.026, 0.072] \approx 0$, indicating that normally distributed noise values propagate through the system to result in a symmetric confidence interval, located about the mean. The value of kurtosis for these distributions was found to be 2.999 ± 0.025, strongly agreeing with the degree of outliers in a Gaussian distribution. In contrast, iteratively extracted results were found to have skew values in the range $[0.399, 1.356]$ as fitted values tend to agglomerate at local minima; combinations of permittivity and thickness which result in maximum quality of fit. Kurtosis of $5.693 \pm 1.604 > 3$ clearly indicates that the distributions are more prone to outliers than a normal distribution.

The Monte Carlo simulations were also used to calculate an average execution time for each iteration of the process. When computed with MATLAB version 8.5.0.197613 (Microsoft Windows 7 Enterprise version 6.1), on an Intel Core i7 3.6 GHz desktop computer, this length of time is 12 s. The total time (measurement and processing) is 15 s (excluding mounting the sample in prealigned holder); a vast reduction in time compared to traditional methods requiring multiple steps to be performed by the metrologist, per sample.

B. Datasets

The data underpinning this research can be located with the identifier.

C. Further Work

Solving systems of linear equations is a task well suited to parallelization on a graphics processing unit. To alleviate the exponential computation time penalty of extending the search-space into extra dimensions for fitting ϵ_r'', further research aims to port existing MATLAB code to a lower level language compatible with NVIDIA's CUDA platform. Subsequently, the formulation of η in Section II-C may be altered to include σ and the accuracy of ϵ_r'' can be investigated with $\max(\text{S21}_{\text{sim}}) < 0$ dB.

IV. CONCLUSION

We have presented a methodology for fast, accurate, and simple permittivity measurements to be made on planar samples

with only an imprecise *a priori* knowledge of geometry. Non-contact, nondestructive testing makes the method well suited to quality control or process monitoring applications requiring high measurement throughput.

REFERENCES

[1] H. Nemec, F. Kadlec, P. Kuzel, L. Duvillaret, and J.-L. Coutaz, "Independent determination of the complex refractive index and wave impedance by time-domain terahertz spectroscopy," *Opt. Commun.*, vol. 260, no. 1, pp. 175–183, Apr. 2006.

[2] T. Tosaka, K. Fujii, K. Fukunaga, and A. Kasamatsu, "Development of complex relative permittivity measurement system based on free-space in 220–330-GHz range," *IEEE Trans. THz Sci. Technol.*, vol. 5, no. 1, pp. 102–109, Jan. 2015.

[3] M. Theuer and J. S. Melinger, "High resolution waveguide terahertz time-domain spectroscopy," *J. Infrared, Millim., THz Waves*, vol. 32, no. 11, pp. 1267–1284, 2011.

[4] J. L. Hesler, Y. Duan, B. Foley, and T. W. Crowe, "THz vector network analyzer measurements and calibration," in *Proc. 21st Int. Symp. Space THz Technol.*, Oxford, U.K., Mar. 2010, pp. 318–320.

[5] D. M. Pozar, *Microwave Engineering*, 4th ed. Hoboken, NJ, USA: Wiley, 2012.

[6] D. K. Ghodgaonkar, V. V. Varadan, and V. K. Varadan, "Free-space measurement of complex permittivity and complex permeability of magnetic materials at microwave frequencies," *IEEE Trans. Instrum. Meas.*, vol. 39, no. 2, pp. 387–394, Apr. 1990.

[7] P. E. Gill, W. Murray, M. A. Saunders, and M. H. Wright, "Procedures for optimization problems with a mixture of bounds and general linear constraints," *ACM Trans. Math. Softw.*, vol. 10, pp. 282–298, 1984.

[8] P. E. Gill, W. Murray, and M. H. Wright, *Numerical Linear Algebra and Optimization*, vol. 1. Reading, MA, USA: Addison-Wesley, 1991.

[9] J. Nocedal and S. Wright, *Numerical Optimization*, 2nd ed. New York, NY, USA: Springer-Verlag, 2006.

[10] S. P. Han, "A globally convergent method for nonlinear programming," *J. Optim. Theory Appl.*, vol. 22, pp. 297–309, 1977.

[11] M. J. D. Powell, "A fast algorithm for nonlinearly constrained optimization calculations," in *Numerical Analysis: Proceedings of the Biennial Conference Held at Dundee, June 28–July 1, 1977*. Berlin, Germany: Springer-Verlag, 1978, pp. 144–157.

[12] Z. Ugray *et al.*, "Scatter search and local NLP solvers: A multistart framework for global optimization," *INFORMS J. Comput.*, vol. 19, no. 3, pp. 328–340, 2007.

[13] M. Naftaly and J. Molloy, "A multi-lab intercomparison study of THz time-domain spectrometers," in *Proc. 2015 40th Int. Conf. Infrared, Millim., THz Waves.*, Hong Kong, Aug. 2015, pp. 1–2.

[14] M. Levinshtein, S. Rumyantsev, and M. Shur, Eds., *Handbook Series on Semiconductor Parameters*, vol. 1. Singapore: World Sci., 1996.

[15] *High Resistivity (HiRes) Silicon For GHz & THz Technology*, rev. 1.1, Topsil, Frederikssund, Denmark, Jan. 2014.

[16] T. H. Isaac, W. L. Barnes, and E. Hendry, "Determining the terahertz optical properties of subwavelength films using semiconductor surface plasmons," *Appl. Phys. Lett.*, vol. 93, no. 24, 2008, Art. no. 241115.

[17] N. M. Ridler and M. J. Salter, "A generalised approach to the propagation of uncertainty in complex s-parameter measurements," in *Proc. 64th ARFTG Microw. Meas. Conf., Fall 2004*, Orlando, FL, USA, Dec. 2004, pp. 1–14.

[18] E. L. Bronaugh and J. D. M. Osburn, "Estimating EMC measurement uncertainty using logarithmic terms (dB)," in *Proc. 1999 IEEE Int. Symp. Electromagn. Compat.*, Seattle, WA, USA, Mar. 1999, pp. 376–378.

[19] N. M. Ridler and R. G. Clarke, "Evaluating the effect of using precision alignment dowels on connection repeatability of waveguide devices at frequencies from 750 GHz to 1.1 THz," in *Proc. 2014 84th ARFTG Microw. Meas. Conf.*, Boulder, CO, USA, Dec. 2014, pp. 1–10.

[20] A. Kazemipour, M. Hudlicka, T. Kleine-Ostmann, and T. Schrader, "A reliable simple method to extract the intrinsic material properties in millimeter/sub-millimeter wave domain," in *Proc. 2014 Conf. Precision Electromagn. Meas.*, Rio de Janeiro, Brazil, Aug. 2014, pp. 576–577.

Jonathan Hammler (S'12–GS'14) received the M.Eng. degree in general engineering (with a specialization in electronic engineering) from Durham University, Durham, U.K., in 2014, where he is currently working toward the Ph.D. degree in electronic engineering.

His recent work has focused on single-pixel imaging schemes and their implementation at terahertz frequencies. His research interests include terahertz devices and spectroscopy, micromanufacturing, and embedded systems development.

Mr. Hammler is a member of the Institution of Engineering and Technology, U.K.

Andrew J. Gallant (M'12) received the B.Sc. degree in applied physics with electronic engineering and the Ph.D. degree in engineering from Durham University, Durham, U.K., in 2000 and 2004, respectively.

He is currently a Postdoctoral Researcher with the Microsystems Technology Group, Durham University, where he was appointed as a Lecturer in 2008 and is currently a Senior Lecturer. His core research activities are focused on the use of micromachining to create new components for the manipulation of terahertz light.

Claudio Balocco (S'05–M'06) was born in Milan, Italy. He received the M.Sc. degree in electronic engineering from the Politecnico di Milano, Milan, in 2002, and the Ph.D. degree in semiconductor nanodevices from the University of Manchester, Manchester, U.K., in 2006.

He is currently a Lecturer in electronics with the School of Engineering and Computing Sciences, Durham University, Durham, U.K., following appointments as a Research Associate with the University of Manchester. His research interests include the design of novel nanodevice architectures and circuits in organic and metal–oxide thin films, ultrafast nanodevices for THz applications, and large-area microfabrication and nanofabrication techniques, as well as transport phenomena in self-assembled quantum dots. More recently, his interest focuses on the interaction of thermal radiation with semiconductor nanodevices with applications envisaged in THz imaging and energy harvesting.